

# Boundary layer heterogeneities can enhance scroll wave stability

Sebastián Echeverría-Alar and Wouter-Jan Rappel

*Department of Physics, University of California, San Diego, California 92093, USA*

(Dated: October 3, 2024)

Electrical scroll waves may cause life-threatening arrhythmias in the heart, and it is therefore important to control their dynamics. We explore how boundary layer heterogeneities affect the scroll wave dynamics in a semidiscrete electrophysiological model. Using simulations, we show that reducing the coupling strength near the boundaries of thin tissues results in a decrease of the angular frequency of the scroll wave, which in turn prevents its meandering instability. Finally, we propose a simplified model that only considers activation in the boundary layer and in one bulk tissue slice, and show that it is able to faithfully capture our numerical observations.

Spatially extended nonlinear systems can exhibit complex spatiotemporal dynamics, often after undergoing an instability [1, 2]. Examples include oscillations in chemical reactions [3], Rayleigh-Bénard convection patterns [4, 5], turbulence in active matter [6], extreme events in lasers [7], and rogue waves in dissipative optical systems [8]. One question that has attracted considerable attention is how this complexity can be controlled and how these instabilities can be suppressed [9–11]. This is a particularly relevant question in the context of cardiac dynamics. Cardiac tissue is a prototypical example of an excitable medium and, under normal conditions, a planar electrical activation front sweeps through the tissue. The accompanied mechanical wave then contracts the heart, resulting in the pumping of blood through the body. However, this planar wave can become unstable and the break-up of the front can result in reentry and the formation of spiral waves. This disorganized behavior leads to serious heart rhythm disorders, including tachycardia and fibrillation [12–14].

In 2D computational domains or tissue sheets, the simplest form of a spiral wave rotates around a core and its tip circumscribes a circular trajectory. Changing the excitability properties of the tissue or parameters in a computational model can trigger a Hopf bifurcation, after which the tip starts to meander, resulting in a more complex trajectory [15, 16]. Cardiac tissue, however, always has a certain thickness and 3D effects may play an important role in the formation of instabilities. The 3D equivalent of a spiral wave is a scroll wave: a stack of 2D spiral waves with a filament that connects the tips in the third ( $z$ ) dimension [17, 18]. In sufficiently thick geometries, filaments incorporate additional degrees of freedom to the spiral waves and their dynamics is therefore richer [18–20]. Filaments, for example, can become unstable, twist, develop line tension, and buckle [20–22]. Conversely, scroll waves confined to thin tissue slabs exhibit dynamics similar to the spiral waves in 2D, i.e., rigid rotation, meandering and break-up [23].

The successful control of scroll wave instabilities in cardiac tissue can treat tachycardia and fibrillation. Nowadays, for example, the consequences of optogenetics manipulation in detailed excitable models are being exten-

sively studied, showing that external continuous forcing are able to control waves and suppress their instabilities [24–27]. However, testing these computational results in human hearts is still a thorny task. In this letter, we demonstrate that the introduction of boundary layer heterogeneities in a thin computational tissue slab can significantly increase the parameter range for which a scroll wave is stable. Specifically, we show that decreasing the coupling strength between cardiac cells near the boundaries of this slab can stabilize scroll waves in the bulk against a meandering instability. Choosing this type of heterogeneity is motivated in part by the fact that heart rhythm disorders are often treated by ablation during which tissue is destroyed by applying heat, cold, or pulsed electric fields through a catheter inserted into the heart. However, ablation often leads to incomplete lesions due to, e.g., insufficient exposure time, and only renders tissue non-conductive up to a certain depth, thus creating a significant transmural heterogeneity in which a region with impaired conduction is sandwiched between conductive and non-conductive tissue [28–31]. Additional motivation comes from boundary heterogeneities that are due to intrinsic properties of the tissue, including fatty zones that are often found on the epicardial surface of the heart [32, 33].

We consider a tissue slab of thickness  $\mathcal{H} \ll L$ , where  $L = 5.08$  cm is the width of the slab, which is oriented in a Cartesian frame with the  $z$  axis in the transmural direction. Along this transmural direction, the slab is symmetrically divided into a boundary layer of size  $l$  and a bulk region of size  $h$ , i.e.,  $\mathcal{H} = h + 2l$  (see Fig. 1A). In the boundary region, the coupling strength between cardiac cells is weaker than in the bulk by a factor  $\alpha < 1$ . This can be incorporated by multiplying the diffusion term in the usual equation for the spread of the transmembrane voltage,  $u$ , by  $\alpha$ . In the continuum description of this equation, numerical simulations can be carried out using, e.g., finite difference stencils that take into account nearest neighbors. In our study we aim to explore a range of  $\alpha$  values without restrictions and, therefore, we will discretize the  $z$ -direction in slices with a thickness corresponding to the size of a cardiomyocyte:  $d_z = 25 \mu\text{m}$  [34].

To model the excitable dynamics of cardiac cells, we employ the following semi-discrete equation;

$$\partial_t u = \mathcal{I}_k D_o \nabla_{\perp}^2 u + C_z - \frac{I_{ion}}{C_m}, \quad (1)$$

where  $C_m$  is the membrane capacitance and  $I_{ion}$  corresponds to the membrane currents. The first term in this equation describes the spatial coupling in the  $x-y$  plane, with  $\mathcal{I}_k$  encoding the heterogeneous coupling strength distribution in the different slices:

$$\mathcal{I}_k = \begin{cases} \alpha, & 0 \leq kd_z < l \cup \mathcal{H} - l < kd_z \leq \mathcal{H} \\ 1, & l \leq kd_z \leq \mathcal{H} - l \end{cases}. \quad (2)$$

Here, the subscript  $k = \{0, \dots, \mathcal{H}/d_z\}$  labels the tissue layer along the transmural direction. This term is a continuum description of the isotropic diffusive process in the  $x-y$  plane and is discretized using a simple 5-point stencil with step size  $\Delta x = 0.0254$  cm. We have verified that choosing smaller values of  $\Delta x$  did not affect our results. The second term describes discrete coupling along the  $z$  direction and is written as:

$$C_z = \frac{D_z}{d_z^2} \left[ \mathcal{Q}_{k+1}(u_{k+1} - u_k) + \mathcal{Q}_{k-1}(u_{k-1} - u_k) \right], \quad (3)$$

where  $\mathcal{Q}_{k+1} = \min(\mathcal{I}_k, \mathcal{I}_{k+1})$  and  $\mathcal{Q}_{k-1} = \min(\mathcal{I}_k, \mathcal{I}_{k-1})$ . We choose an isotropic diffusion coefficient of  $D_o = 0.001$  cm<sup>2</sup>/ms and, consistent with experimental values, a transverse diffusion constant  $D_z$  that is 5 times smaller [35]. The last term,  $f(u, v, w)$ , represents a description of the ion currents governing the cell excitability and is taken from the Fenton-Karma (FK) model [36]. This term depends on several parameters, including ones that control the excitability of the domain (see Section I in the Supplemental Material [35]). Finally, the slab is bounded by non-flux boundary conditions in all directions.

In the homogeneous case ( $\alpha = 1$ ), our model exhibits scroll waves, which can rigidly rotate with a frequency  $\omega_o$ . The tip location, computed using the intersection of equal potential lines from successive time steps [36], is identical in each layer, resulting in a straight filament. Decreasing  $\tau_d$ , a parameter that controls the excitability, the scroll wave starts to rotate faster and eventually undergoes a meandering instability at a critical value  $\tau_d^c = 0.384$ . As a result, the filament will repeat a star-shaped trajectory every 0.5 s. This is shown in Fig. 1B, which plots the trajectory of the filament on the surfaces of the three-dimensional slab as a function of time, indicated by a color code. This bifurcation occurs for exactly the same value in the 2D version of Eq. (1) (i.e.,  $C_z = 0$ ), and is independent of the thickness  $\mathcal{H}$ , at least when  $\mathcal{H} \leq 34d_z$ .

Introducing a boundary layer heterogeneity, parameterized by decreasing  $\alpha$  in top and bottom slices of the slab, reduces the critical value of  $\tau_d$ ;  $\tau_d^{c*}$ . This is illustrated in Fig. 1C, where we instantaneously decrease  $\alpha$

from 1 to 0.004 at time  $t_{het}$  using the same value of  $\tau_d$  as in Fig. 1B. Plotting the tip trajectory in the slice bordering the heterogeneity reveals that the introduction of the boundary layer stabilizes the scroll wave, which eventually exhibits a circular rotation. We note that the heterogeneity does not need to cover the whole boundary slice to suppress the meandering instability (see Fig. 1 in the Supplemental Material [35]).

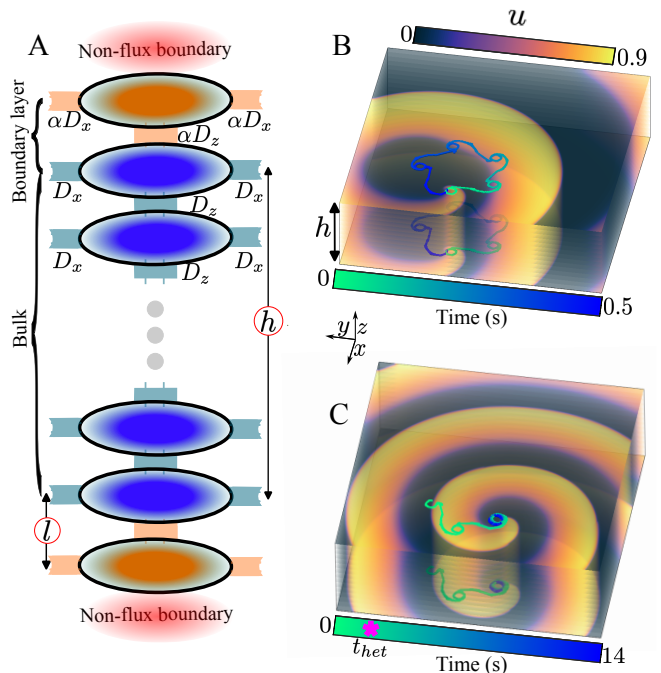


FIG. 1. Boundary layer effect in numerical simulations in a slab with thickness  $\mathcal{H} = 14d_z$  and  $l = d_z$ . (A) Schematic representation of the discrete coupling between cardiomyocytes along the transmural direction. (B) Star-like tip trajectories and the variable  $u$ , representing the transmembrane voltage, in the top and bottom slice for the homogeneous case at  $\tau_d = 0.382$  (the other parameters are given in Section I in the Supplemental Material [35]). (C) As in B with a boundary layer heterogeneity of strength  $\alpha = 0.004$  introduced at time  $t_{het}$ . After several rotations, the meandering scroll wave stabilizes and exhibits a circular motion in every slice.

To systematically explore the stabilization of scroll waves in the presence of boundary layer heterogeneities of size  $d_z$ , we carry out numerical integration of Eq. (1) starting with a rigidly rotating scroll wave and  $\tau_d^o = 0.390$ . We then decrease this parameter in steps of 0.001 ms until we trigger the meandering instability at  $\tau_d = \tau_d^{c*}$ . For each value of  $\tau_d$ , we wait 15 rotations ( $15T_{rot}$ ) of the scroll wave before decreasing its value again. We first carry out these simulations in the absence of a heterogeneity, which show that the frequency increases linearly as  $\tau_d$  decreases (open symbols and red line in Fig. 2A). Repeating these simulations in the presence of the heterogeneity of Fig. 1 reveals that the heterogeneity slows down the scroll wave and that the me-

andering bifurcation now occurs for a different critical value  $\tau_d^{c*}$  (closed symbols in Fig. 2A). Note, however, that the linear dependence between the frequency and  $\tau_d$  is almost conserved in the heterogeneous case, but with a slight deviation within the range  $[\tau_d^{c*}, \tau_d^c]$ , as indicated by the dashed line in Fig. 2A.

Next, to elucidate the role of the slab thickness and the strength of the coupling at the boundaries in scroll wave stabilization, we systematically varied  $\mathcal{H}$  and  $\alpha$  and determined  $\tau_d^{c*}$  and the angular frequency at  $\tau_d^o$ . The results can be summarized in two phase diagrams. The first one shows the increase in stability  $\Delta\tau_d^c/\tau_d^c$ , where  $\Delta\tau_d^c = \tau_d^{c*} - \tau_d^c$  (Fig. 2B). The second one displays the frequency ratio  $\omega/\omega_o$  at  $\tau_d^o$  (Fig. 2C), which is a signature of the boundary layer effect in the scroll wave motion. Note that for illustration purposes, these phase diagrams are shown in the  $\tilde{\alpha} - \mathcal{H}/d_z$  space, with  $\tilde{\alpha} = \log(\alpha) + c$ .

The phase diagrams illustrate that an enhancement of stability is correlated with a reduction in the rotational frequency of the waves. The enhancement of stability becomes larger for thinner slabs, which can be expected since the boundary layer becomes proportionally larger. This is also the reason why a larger boundary layer size ( $l = 2d_z$ ) results in increased bulk stabilization (see Fig. 2 in the Supplemental Material [35]). A relevant division in the phase diagrams is at  $\tilde{\alpha} = \tilde{\alpha}_f$ , where  $\alpha_f = 0.002$  (dashed line in Figs. 2B-C); for  $\alpha < \alpha_f$ , wave propagation fails towards the boundaries. Interestingly, when the boundaries can be fully excited and the tissue slab is sufficiently thin,  $\mathcal{H}/d_z \leq 6$ , we found a region where the introduction of the heterogeneities terminates the spiral wave dynamics in the bulk (gray areas in Figs. 2B-C).

To gain insights into the mechanisms underlying the suppression of the meandering instability, we analyze separately the cases  $\alpha < \alpha_f$  and  $\alpha > \alpha_f$ . In the former case,  $\omega$  varies linearly as a function of  $\alpha$  for all values of  $\mathcal{H}$  (Fig. 3A), and also the maximum of the potential in the boundary slice,  $u_0$ , increases linearly with  $\alpha$ , until  $\alpha = 5 \times 10^{-4}$  (Fig. 3B), but is significantly lower than the maximum value in the bulk. We therefore call this the *leakage* regime: wave propagation in the bulk is not enough to fully excite the boundary slices and the potential in the bulk leaks into the boundary layer. This leakage is illustrated in Fig. 3C, which shows a snapshot of  $u$  in the boundary layer (left column), the slice next to the boundary  $u_1$  (middle column), and the difference  $u_1 - u_0 \approx u_1$  (right column).

The linear decrease in angular frequency as a function of  $\tau_d$  can be analytically addressed in the case  $\alpha < \alpha_f$ . For this, we consider a tissue slab of size  $\mathcal{H} = 2d_z$ , i.e., one bulk slice sandwiched by two boundary layers. As a consequence of the transmembrane voltage difference  $u_1 \gg u_0$ , the dynamics can be analyzed by considering only the bulk slice  $u_1$ , where  $C_z = -2\alpha D_z/d_z^2 u_1 + \mathcal{O}(\alpha u_0)$ . Note that the leaking effect towards the boundaries is analogous to a loss of

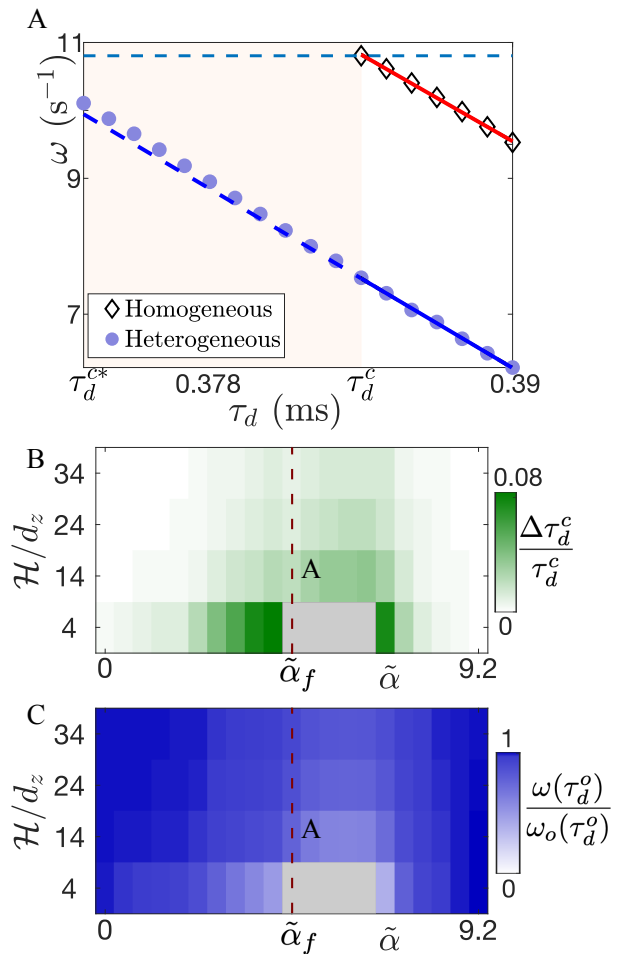


FIG. 2. Control of scroll wave meandering instability. (A) Angular frequency as a function of excitability parameter  $\tau_d$  in a tissue slab of thickness  $\mathcal{H} = 14d_z$  in homogeneous (open diamonds) and heterogeneous (closed circles) conditions. The strength of the heterogeneity is  $\alpha = 0.004$  and its size is  $l = d_z$ . The shaded area represent the enhancement of stability of the scroll waves, where  $\tau_d^c = 0.384$  ms and  $\tau_d^{c*} = 0.373$  ms. The blue dashed line emphasizes the critical value of frequency at which the meandering transition occurs in the homogeneous scenario. The solid lines indicate linear fits ( $p < 0.05$ ). (B-C) Phase diagrams in  $\tilde{\alpha} - \mathcal{H}/d_z$  space showing the level of enhancement of stability  $\Delta\tau_d^c/\tau_d^c$  and the frequency ratio  $\omega/\omega_o$  at  $\tau_d^o = 0.390$  ms, respectively.  $\tilde{\alpha} = \log(\alpha) + c$ , where  $c = 10.82$ , and  $\tilde{\alpha}_f$  is the value for propagation failure.

excitability in the medium controlled by  $\alpha$ . Similar to previous works [21, 37], we can perform a weakly non-linear analysis around the rigidly rotating spiral wave solution  $\mathbf{u}_1^{[0]} = \{u_1, v_1, w_1\}^{[0]}$ . Introducing the ansatz  $\mathbf{u}_1 = \mathbf{u}_1^{[0]} + \alpha\mathbf{u}_1^{[1]} + \dots$ ,  $\omega = \omega_o + \Delta\omega + \dots$  into Eq. (1) in the rotational frame  $\partial_t = \omega\partial_\theta$  and assuming that  $\Delta\omega \sim \alpha$ , we find that  $\Delta\omega = -2D_z A\alpha/Bd_z^2$ , where  $A$  and  $B$  are positive constants (see Section IV in the Supplemental Material [35]). Consistent with our numerical results, this analysis shows that the decrease of excitability in the

bulk, governed by the boundary layer heterogeneities, induces a reduction of the angular frequency of the scroll wave. Although this analysis is only valid when  $\tau_d > \tau_d^c$ , our numerical results support the idea that this angular frequency reduction plays a role in the delay of the meandering instability (Figs. 2B-C).

When  $\alpha > \alpha_f$ , wave propagation in the bulk is able to fully excite the boundary layers and the equilibrium of the system drastically changes, as depicted in Fig. 3D. At this transition, the maximum value of  $u_0$  abruptly changes from a low value ( $\approx 0.14$ ) to a high value ( $\approx 0.92$ ) (see Fig. 3 in the Supplemental Material [35]). In this case, the bulk excites the boundary, and at the same time the boundary regulates the bulk. This *feedback* regime is characterized by a non-trivial voltage difference at the bulk-boundary layer interface (see right column in Fig. 3D), where the bulk scroll wave drives the spiral wave at the boundary.

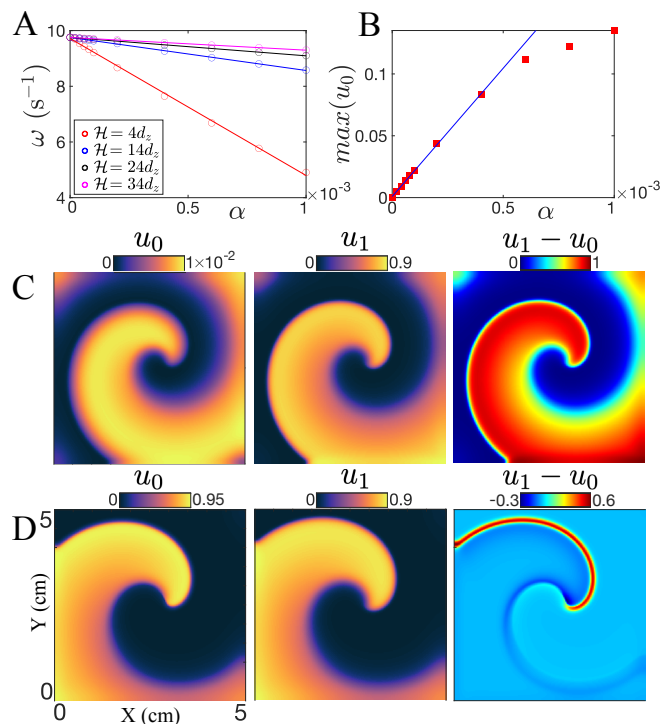


FIG. 3. Dynamical regimes of scroll wave solutions. (A) Angular frequency as a function of  $\alpha$  for different different slab thicknesses in the leakage regime. The variations of the scroll wave frequency is linear ( $p < 0.05$ ) in this limit. (B) The increase of  $\alpha$  produces a linear ( $p < 0.05$ ) increase in Maximum voltage in the boundary slice  $u_0$  as a function of  $\alpha$  until  $\alpha = 5 \times 10^{-4}$  ( $H/d_z = 14$ ). (C-D) Voltage  $u_0$ ,  $u_1$  and their difference  $u_1 - u_0$  in the leakage (C) and feedback regimes (D). Note that there is a two order of magnitude difference between  $u_0$  and  $u_1$  in the leakage regime. The size of the boundary layer is  $d_z$ .

For all values of  $\alpha$  and  $h$ , our numerical simulations show that in the bulk of the slab the term  $\mathcal{C}_z = D_z \partial_{zz} u$  is approximately independent of  $z$ . Then, in the rotational

frame of reference, one can solve a Laplace equation to find  $u$ . Notice that we have introduced the continuum limit along  $z$ , which is valid in the bulk. To incorporate the boundary conditions, we use the symmetry of our geometrical setup (Fig. 1A). Specifically, we consider the middle slice as a wall dividing the tissue slab in two symmetric halves. The Laplace equation can thus be solved in one of these halves with the Dirichlet boundary condition  $u = u_m$  at  $z = 0$ , where  $u_m = u_{\mathcal{H}/2d_z}$  is the transmembrane voltage at the middle of the tissue slab, and the Neumann boundary condition  $\partial_z u = \alpha(u_0 - u_1)/d_z$  at  $z = h/2$ . The solution, back in discrete form, gives the transmembrane voltage in each slice of the bulk

$$u_k = u_m + \chi_k(u_0 - u_m), \quad (4)$$

where  $\chi_k = 4\alpha(kd_z)^2/(4hd_z + \alpha h^2)$ . The above equation can be introduced in Eq. (1), reducing the full 3D equations into a far simpler 2-slices model

$$\begin{aligned} \partial_t u_m &= D_o \nabla_{\perp} u_m + f(\mathbf{u}_m) + 2 \frac{D_z}{d_z^2} \chi_{m+1} (u_0 - u_m) \\ \partial_t u_0 &= \alpha D_o \nabla_{\perp} u_0 + f(\mathbf{u}_0) + \alpha \frac{D_z}{d_z^2} (1 - \chi_1) (u_m - u_0), \end{aligned} \quad (5)$$

where  $\mathbf{u}_m = \{u_m, v_m, w_m\}$  and  $\mathbf{u}_0 = \{u_0, v_0, w_0\}$ . Numerical integrations of Eq. (5) show perfect agreement with the full 3D model Eq. (1), in terms of  $\omega$ , delay of the meandering instability  $\Delta\tau_d^c$  (Fig. 4A), and even in the core size of the scroll wave at the middle slice  $R_{\mathcal{H}/2d_z}$  (Fig. 4B). We highlight that in the feedback regime, the bulk, represented by  $\mathbf{u}_m$ , experiences not only a decrease in excitability,  $-2D_z \chi_{m+1} u_m / d_z^2$ , but also a continuous forcing from the boundary given by  $2D_z \chi_{m+1} u_0 / d_z^2$ .

In summary, we have shown the possibility of increasing the stability of scroll waves within thin tissue slabs due to the presence of boundary layer heterogeneities. The delay of the meandering mode is associated with a slowing down of scroll waves solutions, which can be explained, depending on the strength of the conduction decrease, either by a reduction of excitability or by a feedback between bulk and boundaries. The full 3D system can be reduced into a forced model for the middle and one of the boundary slices. Our work paves the way for new control techniques of scroll waves in cardiac research, where the incorporation of static boundary heterogeneities can help bulk waves to self-regulate themselves. The latter could be useful in finding new ablation techniques with minimal tissue destruction. Possible future directions are to extend our findings into more complicated spatiotemporal regimes and determine whether the introduction of boundary layer heterogeneities is able to suppress scroll wave break-up.

We thank Yuhai Tu, Mahesh Kumar Mulimani and Michael Reiss for fruitful discussions. This work was financially supported by NIH R01 HL122384. S.E.-A. acknowledges the financial support of Beca Chile 74230063.



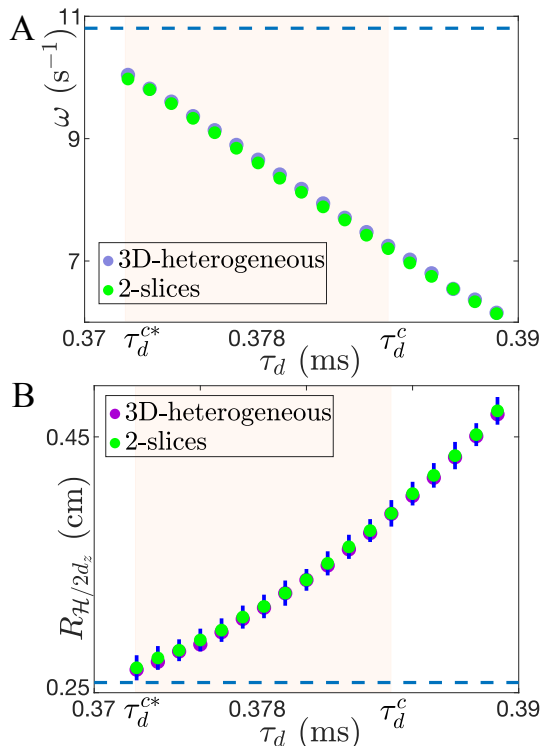


FIG. 4. Comparison of the angular frequency (A) and core radius (B) between the full 3D heterogeneous model in a tissue slab of thickness  $\mathcal{H} = 14d_z$ , with a boundary heterogeneity of  $\alpha = 0.005$ , and the 2-slices model. Blue bars indicate standard deviation of  $R_{\mathcal{H}/2d_z}$  associated to errors in the tip detection algorithm. The segmented lines correspond to the critical  $\omega$  and  $R_{\mathcal{H}/2d_z}$  values in the homogeneous case.

[1] M. C. Cross and P. C. Hohenberg, *Reviews of modern physics* **65**, 851 (1993).  
[2] M. Cross and H. Greenside, *Pattern formation and dynamics in nonequilibrium systems* (Cambridge University Press, 2009).  
[3] A. Zaikin and A. Zhabotinsky, *Nature* **225**, 535 (1970).  
[4] D. A. Egolf, I. V. Melnikov, W. Pesch, and R. E. Ecke, *Nature* **404**, 733 (2000).  
[5] M. Cross and D. Meiron, *Physical review letters* **75**, 2152 (1995).  
[6] B. Martínez-Prat, J. Ignés-Mullol, J. Casademunt, and F. Sagués, *Nature physics* **15**, 362 (2019).  
[7] V. Pammi, M. Clerc, S. Coulibaly, and S. Barbay, *Physical Review Letters* **130**, 223801 (2023).  
[8] M. Tlidi and M. Taki, *Advances in Optics and Photonics* **14**, 87 (2022).  
[9] D. M. Walkama, N. Waisbord, and J. S. Guasto, *Physical review letters* **124**, 164501 (2020).  
[10] S. B. Ivars, M. Botey, R. Herrero, and K. Staliunas, *Physical Review A* **105**, 033510 (2022).  
[11] K. Beppu and J. Timonen, *Communications Physics* **7**,

216 (2024).  
[12] A. Panfilov, *Physical review letters* **88**, 118101 (2002).  
[13] A. Karma, *Annu. Rev. Condens. Matter Phys.* **4**, 313 (2013).  
[14] W.-J. Rappel, *Physics reports* **978**, 1 (2022).  
[15] D. Barkley, M. Kness, and L. S. Tuckerman, *Physical Review A* **42**, 2489 (1990).  
[16] D. Barkley, *Physical Review Letters* **68**, 2090 (1992).  
[17] A. T. Winfree, *Science* **181**, 937 (1973).  
[18] L. M. Pismen, *Vortices in nonlinear fields: from liquid crystals to superfluids, from non-equilibrium patterns to cosmic strings*, Vol. 100 (Oxford University Press, 1999).  
[19] J. P. Keener, *Physica D: Nonlinear Phenomena* **31**, 269 (1988).  
[20] J. P. Keener and J. J. Tyson, *SIAM review* **34**, 1 (1992).  
[21] H. Henry and V. Hakim, *Physical Review E* **65**, 046235 (2002).  
[22] A. Pertsov, R. Aliev, and V. Krinsky, *Nature* **345**, 419 (1990).  
[23] S. Alonso, M. Bär, and A. V. Panfilov, *Bulletin of Mathematical Biology* **75**, 1351 (2013).  
[24] S. Hussaini, A. Mamyraim Kyzy, J. Schröder-Schetelig, S. Lädke, V. Venkatesan, L. Diaz-Maue, R. Quiñonez Uribe, C. Richter, V. Biktashev, R. Majumder, *et al.*, *Chaos: An Interdisciplinary Journal of Nonlinear Science* **34** (2024).  
[25] T.-C. Li, W. Zhong, B.-q. Ai, W.-J. Zhu, B.-W. Li, A. V. Panfilov, and H. Dierckx, *Physical Review E* **108**, 034218 (2023).  
[26] S. Hussaini, V. Venkatesan, V. Biasci, J. M. Romero Sepúlveda, R. A. Quiñonez Uribe, L. Sacconi, G. Bub, C. Richter, V. Krinski, U. Parlitz, *et al.*, *Elife* **10**, e59954 (2021).  
[27] T. Bruegmann, P. M. Boyle, C. C. Vogt, T. V. Karathanos, H. J. Arevalo, B. K. Fleischmann, N. A. Trayanova, P. Sasse, *et al.*, *The Journal of clinical investigation* **126**, 3894 (2016).  
[28] E. Bugge, I. A. Nicholson, and S. P. Thomas, *European journal of cardio-thoracic surgery* **28**, 76 (2005).  
[29] R. Jiang, E. Buch, J. Gima, G. A. Upadhyay, H. M. Nayak, A. D. Beaser, Z. Aziz, K. Shivkumar, and R. Tung, *Heart rhythm* **16**, 1151 (2019).  
[30] A. J. Rogers, R. T. Borne, G. Ho, W. H. Sauer, P. J. Wang, S. M. Narayan, L. Zheng, and D. T. Nguyen, *Journal of cardiovascular electrophysiology* **31**, 1687 (2020).  
[31] H. Nakagawa, Q. Castellvi, R. Neal, S. Girouard, J. Laughner, A. Ikeda, M. Sugawara, Y. An, A. A. Hussein, S. Nakhla, *et al.*, *Circulation: Arrhythmia and Electrophysiology* **17**, e012026 (2024).  
[32] A. S. Antonopoulos and C. Antoniadis, *The Journal of physiology* **595**, 3907 (2017).  
[33] A. C. Ernault, V. M. Meijborg, and R. Coronel, *Journal of the American College of Cardiology* **78**, 1730 (2021).  
[34] P. C. Hsieh, M. E. Davis, L. K. Lisowski, and R. T. Lee, *Annu. Rev. Physiol.* **68**, 51 (2006).  
[35] Supplemental Material.  
[36] F. Fenton and A. Karma, *Chaos: An Interdisciplinary Journal of Nonlinear Science* **8**, 20 (1998).  
[37] S. Setayeshgar and A. J. Bernoff, *Physical review letters* **88**, 028101 (2001).

# Supplemental Material on "Boundary layer heterogeneities can enhance scroll wave stability"

Sebastián Echeverría-Alar and Wouter-Jan Rappel  
 Department of Physics, University of California, San Diego, California, 92093, USA  
 (Dated: October 3, 2024)

## I. Electrophysiological model

The reaction-diffusion model chosen to explore the effects of boundary layer heterogeneities in the stability of scroll waves, is a semi-discrete version of the well-established Fenton-Karma (FK) model [1]. In this model, the evolution of the transmembrane action potential  $u$  obeys

$$\partial_t u = \mathcal{I}_k D_o \nabla_{\perp}^2 u + C_z - \frac{I_{ion}}{C_m}, \quad (1)$$

where  $D_o$  is a diffusion coefficient,  $\mathcal{I}_k$  is a function controlling the heterogeneity distribution in each slice,  $C_z$  represents the discrete coupling along the  $z$ -direction, which is controlled by the coupling strength  $D_o/5d_z^2$ ,  $C_m$  is the membrane capacitance, and  $I_{ion} = I_{fi} + I_{so} + I_{si}$  is the sum of membrane currents. These currents depends on electrophysiological parameters and describe the following excitable dynamics

$$I_{fi}(u, v) = -\frac{v}{\tau_d} \Theta(u - u_c)(1 - u)(u - u_c), \quad (2)$$

$$I_{so}(u) = \frac{u}{\tau_o} \Theta(u_c - u) + \frac{1}{\tau_r} \Theta(u - u_c), \quad (3)$$

$$I_{si}(u, w) = -\frac{w}{\tau_{si}} (1 + \tanh(k(u - u_{c,si}))). \quad (4)$$

The gating variables  $v$  and  $w$  evolve according to local dynamics:

$$\partial_t v = \frac{1}{\tau_v^-(u)} \Theta(u_c - u)(1 - v) - \frac{1}{\tau_v^+} \Theta(u - u_c)v, \quad (5)$$

$$\partial_t w = \frac{1}{\tau_w^-} \Theta(u_c - u)(1 - w) - \frac{1}{\tau_w^+} \Theta(u - u_c)w, \quad (6)$$

where  $\tau_v^-(u) = \Theta(u - u_v)\tau_{v1}^- + \Theta(u_v - u)\tau_{v2}^-$ . In our simulations, all electrophysiological parameters are kept constant (and listed in Table I), except  $\tau_d$ , which controls the excitability in Eq. (1), which is used as the bifurcation parameter to go from rigidly rotating to meandering scroll waves. Note that both types of waves are equilibria of Eqs. (1)-(6). The system of equations are numerically integrated in a slab of size  $L \times L \times \mathcal{H}$  (see Fig.1 of the main text). In each  $x - y$  slice, we use a forward Euler method with time step  $\Delta t$  and the Laplacian is approximated by a 5-point stencil with a spatial discretization size  $\Delta x$ . In the transmural ( $z$ ) direction, we used the discretization reported in the main text.

TABLE I. Electrophysiological and numerical parameters used for all numerical simulations of Eqs. (1)-(6) in the main text. The parameters with no units are dimensionless.

$C_m$ ( $\mu\text{F}/\text{cm}^2$ )	$u_c$	$\tau_o$ (ms)	$\tau_r$ (ms)	$\tau_{si}$ (ms)	$k$	$u_{c,si}$	$u_v$	$\tau_{v1}^-$ (ms)	$\tau_{v2}^-$ (ms)	$\tau_v^+$ (ms)	$\tau_w^-$ (ms)	$\tau_w^+$ (ms)	$L$ (cm)	$\Delta x$ (mm)	$d_z$ ( $\mu\text{m}$ )	$\Delta t$ (ms)
1	0.13	9	33	29	15	0.5	0.04	9	8	3.3	60	250	5.08	0.254	25	0.01

## II. Scroll wave stabilization in the presence of a localized transmural heterogeneity

In the main text, we focused on the simple scenario in which the heterogeneity distributions are uniform in the  $x-y$  directions and cover the whole slice. Here, we ask ourselves if it is possible to stabilize the meandering instability with a localized heterogeneity in the  $x-y$  plane and if this heterogeneity can trap a meandering scroll wave. To answer this question, we introduce a circular heterogeneity in the upper and lower slice of a  $2L \times 2L \times \mathcal{H}$  slab. The diameter of the heterogeneity is taken as  $L_{het} = 4$  cm and the reduction of conduction is parameterized by  $\alpha = 0.004$ . Note that this reduction now occurs not only in the transmural direction but also in the  $x-y$  plane. Figure 1 illustrates snapshots of a spiral wave that is meandering in the absence of a boundary layer heterogeneity ( $\tau_d = 0.382$ ). The introduction of the circular heterogeneity, however, stabilizes and traps the meandering wave: once the filament enters the heterogeneous region (circular shaded region), it starts to exhibit locally a rigid rotation behavior ( $t_3$ ) and after a transient of around  $18T_{rot}$ , the final equilibrium state is a rigidly rotating scroll wave ( $t_4$ ).

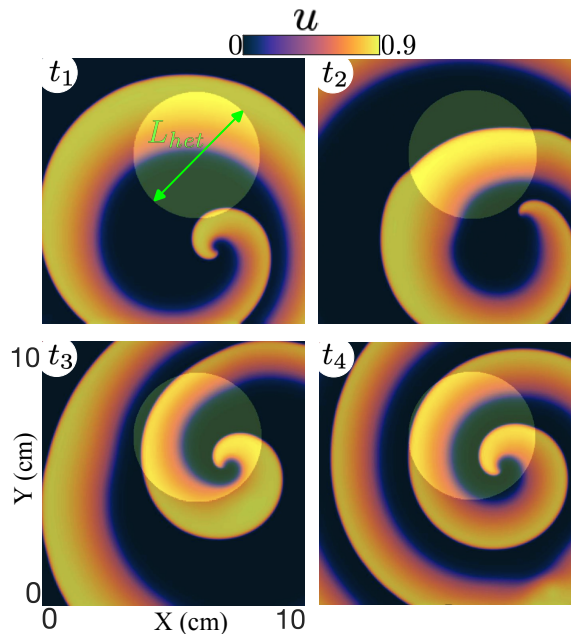


FIG. 1. Scroll wave interacting with a localized boundary layer heterogeneity in the FK model. The temporal sequence  $t_1 = 0 < t_2 < t_3 < t_4 = 19T_{rot}$ , with  $T_{rot} = 122$  ms, describes the trapping of a scroll wave observed at the middle of a tissue slice with thickness  $\mathcal{H} = 15d_z$ . The boundary layers have a volume  $\pi L_{het}^2 l/4$  and in this particular simulation  $l = d_z$  and  $L_{het} = 4$  cm.

## III. Bigger boundary layer

In the main text, we focused on the scroll wave stabilization using boundary layer heterogeneities of size  $l = d_z$ . However, we have verified that the delay of the meandering instability by slowing down scroll waves is present when  $l > d_z$ . Figure 2 shows the change in the enhancement of stability of scroll waves,  $\Delta\tau_d^c = \tau_d^{*c} - \tau_d^c$ , normalized by  $\tau_d^c$  in a tissue slab of thickness  $\mathcal{H} = 14d_z$  in the presence of boundary layers of size  $l = d_z$  and  $l = 2d_z$ . In the leakage regime,  $\alpha < \alpha_f$ , both curves are essentially identical. In the feedback regime ( $\alpha > \alpha_f$ ), however, the enhancement of stability is larger for the thicker boundary layer heterogeneity. This is simply related to the fact that the ratio  $2l/h$  becomes closer to 1.

## IV. Weakly nonlinear analysis in the leakage regime $\alpha < \alpha_f$

Due to the symmetry of our problem, one can write equations only for one half of the tissue slab. For example, in the case of a slab with three slices and with a heterogeneity of size  $l = d_z$  and strength  $\alpha$ , we can write 6 2D-equations

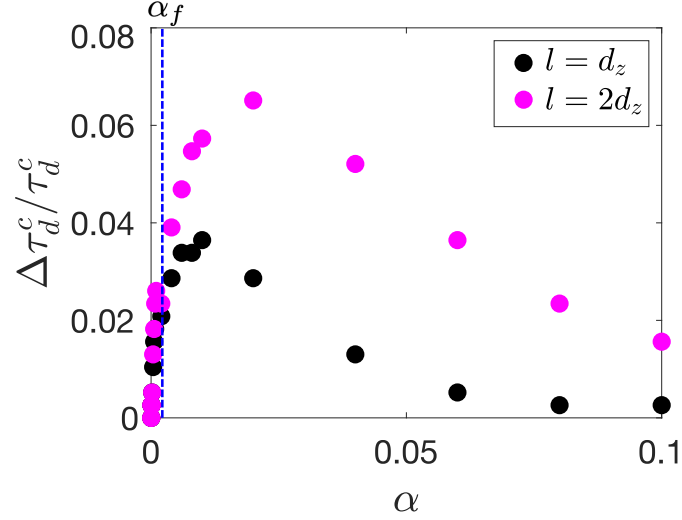


FIG. 2. Effects of boundary layer size  $l$  in the enhancement of scroll wave stability  $\Delta\tau_d^c/\tau_d^c$ . The segmented blue line indicates the propagation failure along the transmural direction  $\alpha_f = 0.002$ .

$$\begin{aligned}
 \partial_t u_1 &= D_x \nabla_{\perp} u_1 + 2\alpha \frac{D_z}{d_z^2} (u_0 - u_1) - \frac{I_{ion}}{C_m} \\
 \partial_t v_1 &= F(u_1, v_1) \\
 \partial_t w_1 &= G(u_1, w_1) \\
 \partial_t u_0 &= \alpha D_x \nabla_{\perp} u_0 + \alpha \frac{D_z}{d_z^2} (u_1 - u_0) - \frac{I_{ion}}{C_m} \\
 \partial_t v_0 &= F(u_0, v_0) \\
 \partial_t w_0 &= G(u_0, w_0).
 \end{aligned} \tag{7}$$

Here the index 0 refers to the boundary layer and the index 1 refers to the bulk. In the leakage regime,  $u_1 \gg u_0$ , we only need to take into account equations in the bulk since  $u_0 - u_1 \approx -u_1$ . In other words, the bulk receives a negligible amount of current from the boundary.

Our analysis relies on the linearization of some of the nonlinear terms in Eq. (7). Therefore, we need to smooth the Heaviside functions and we replace these functions by sigmoidal functions;  $\Theta(q) = (1 + \tanh(s_f q))/2$  with  $s_f = 15$ . This changes the excitability of the system and, therefore, the behavior and shape of spiral waves in the parameter set of Table I. However, it is still possible to trigger a meandering instability, now at  $\tau_d^c = 0.348$  instead of 0.384 as for the Fenton-Karma model considered in the main text.

We numerically solve the bulk part of Eq. (7) with  $\alpha = 0$  and smoothed Heavisides in polar coordinates where the initial condition is a spiral wave generated from direct numerical simulations in a cartesian grid, which is interpolated to a polar grid centered at the spiral core center. The polar geometry consist of a disk of radius  $R_{disk} = 2.29$  cm with a spatial discretization  $\Delta r = \Delta x$  in the radial direction and 128 points along the angular ( $\theta$ ) direction. In the radial direction a 4-point stencil is used with non-flux boundary conditions at  $r = 0$  and  $r = R_{disk}$ , and a spectral method is used to discretize the angular terms of the Laplacian [2]. The equations are integrated in time with an explicit Euler method with  $\Delta t = 0.0001$  ms. The steady state, achieved after 15 rotations of the spiral wave at  $\tau_d = 0.355$ , is described by the spiral solution  $\{u_1, v_1, w_1\}^{[0]}$  with an angular frequency  $\omega_o$ .

In the following, we perform a weakly nonlinear analysis around the homogeneous solution in the rotational frame of reference  $\partial_t = \omega \partial_{\theta}$  to characterize how the frequency  $\omega$  varies as a function of the heterogeneity strength  $\alpha$ . Introducing the ansatz  $\mathbf{u}_1^{[0]} + \alpha \mathbf{u}_1^{[1]} + \dots$ ,  $\omega = \omega_o + \Delta\omega + \dots$  in the bulk terms of Eq. (7) and considering that  $\Delta\omega \sim \alpha$ ,



we find at  $\mathcal{O}(\alpha)$  a linear system of equations for the nonlinear correction;  $\mathcal{L}\{u_1, v_1, w_1\}^{[1]} = \mathbf{b}$  where

$$\mathcal{L} = \begin{pmatrix} D_x \nabla_{\perp}^2 + \omega_o \partial_{\theta} - \frac{\partial \hat{I}_{ion}}{\partial u_1} & \frac{\partial \hat{I}_{ion}}{\partial v_1} & \frac{\partial \hat{I}_{ion}}{\partial w_1} \\ \frac{\partial \hat{F}}{\partial u_1} & \omega_o \partial_{\theta} + \frac{\partial \hat{F}}{\partial v_1} & 0 \\ \frac{\partial \hat{G}}{\partial u_1} & 0 & \omega_o \partial_{\theta} + \frac{\partial \hat{G}}{\partial w_1} \end{pmatrix} \quad (8)$$

and

$$\mathbf{b} = -\Delta\omega \partial_{\theta} \begin{pmatrix} u_1 \\ v_1 \\ w_1 \end{pmatrix}^{[0]} + 2\alpha \frac{D_z}{d_z^2} \begin{pmatrix} u_1 \\ 0 \\ 0 \end{pmatrix}^{[0]}. \quad (9)$$

The terms  $\hat{I}_{ion}$ ,  $\hat{F}$  and  $\hat{G}$  in Eq. (8) depend on the smoothed version of the Heaviside functions. To solve the linear system, we must introduce an inner product to apply a solvability condition, i.e., the linear equation will have solution if and only if  $\mathbf{b}$  is orthogonal to the  $Ker\{\mathcal{L}^{\dagger}\}$ . Based on previous studies [3], we consider the inner product  $\langle \mathbf{g} | \mathbf{h} \rangle = \int \int \mathbf{f} \cdot \mathbf{g} r dr d\theta$ , and the elements of the kernel  $Ker\{\mathcal{L}^{\dagger}\} = \{\bar{u}_1, \bar{v}_1, \bar{w}_1\}$  are calculated numerically with a precision  $\mathcal{O}(10^{-3})$ . Finally, we apply the solvability condition  $\langle \{\bar{u}_1, \bar{v}_1, \bar{w}_1\} | \mathbf{b} \rangle = 0$  and obtain

$$\Delta\omega = 2\alpha \frac{D_z}{d_z^2} \frac{\langle \{\bar{u}_1, \bar{v}_1, \bar{w}_1\} | \{u_1, 0, 0\}^{[0]} \rangle}{\langle \{\bar{u}_1, \bar{v}_1, \bar{w}_1\} | \partial_{\theta} \{u_1, v_1, w_1\}^{[0]} \rangle} = 2\alpha \frac{D_z}{d_z^2} \frac{A}{B}, \quad (10)$$

with  $A/B = -0.81$ .

### V. Transition at $\alpha = \alpha_f$

When  $\alpha > \alpha_f$ , wave propagation is possible from the bulk to the boundary, which is characterized by a sharp transition in the maximum value of the boundary transmembrane voltage  $u_0$  as shown in Fig. 3.

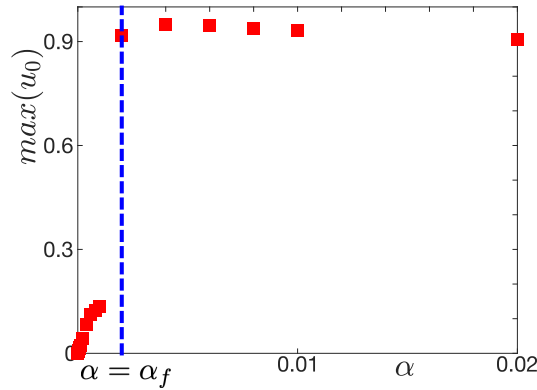


FIG. 3. Maximum boundary voltage as a function of  $\alpha$  in both leakage and feedback regimes.

[1] F. Fenton and A. Karma, *Chaos: An Interdisciplinary Journal of Nonlinear Science* **8**, 20 (1998).

[2] B. Sandstede and A. Scheel, *Spiral waves: linear and nonlinear theory*, 1413 (American Mathematical Society, 2023).

[3] H. Henry and V. Hakim, *Physical Review E* **65**, 046235 (2002).